Nuclear Engineering and Technology 52 (2020) 1571–1578

Contents lists available at ScienceDirect

Nuclear Engineering and Technology

journal homepage: www.elsevier.com/locate/net

Original Article

# Investigating the effects of confining pressure on graphite material failure modes and strength criteria

Yanan Yi [a], Guangyan Liu [a], Tongzhen Xing [a], Guang Lin [a], Libin Sun [b], Li Shi [b], Shaopeng Ma [a, *]

[a] School of Aerospace Engineering, Beijing Institute of Technology, Beijing, 100081, China
[b] Institute of Nuclear and New Energy Technology, Tsinghua University, Beijing, 100084, China

ARTICLE INFO

*Article history:*
Received 20 September 2019
Received in revised form
25 November 2019
Accepted 5 December 2019
Available online 20 December 2019

*Keywords:*
Graphite
Confining pressure
Triaxial strength
Young's modulus
Failure modes
Strength criteria

ABSTRACT

As a critical material in very/high-temperature gas-cooled reactors, graphite material directly affects the safety of the reactor core structures. Owing to the complex structures of graphite material in reactors, the material typically undergoes complex stress states. It is, therefore, necessary to study its mechanical properties, failure modes, and strength criteria under complex stress states so as to provide guidance for the core structure design. In this study, compressive failure tests were performed for graphite material under the condition of different confining pressures, and the effects of confining pressure on the triaxial compressive strength and Young's modulus of graphite material were studied. More specifically, graphite material based on the fracture surfaces and fracture angles, the graphite specimens were found to exhibit four types of failure modes, i.e., tension failure, shear-tension failure, tension-shear failure and shear failure, with increasing confining pressure. In addition, the Mohr strength envelope of the graphite material was obtained, and different strength criteria were compared. It showed that the parabolic Mohr-Coulomb criterion is more suitable for the strength evaluation for the graphite material.
© 2019 Korean Nuclear Society, Published by Elsevier Korea LLC. This is an open access article under the CC BY-NC-ND license (http://creativecommons.org/licenses/by-nc-nd/4.0/).

## 1. Introduction

Graphite material in very/high-temperature gas-cooled reactors (V/HTRs) is a quasi-brittle synthetic material with complex microstructures comprised of fine petroleum coke particles and coal-based binder pitch. It is usually manufactured by using special processes such as isobaric vibration or high-temperature graphitization [1]. As the neutron moderator, reflector, and structural support of V/HTRs, graphite material plays a key role in maintaining normal reactor operation [2,3]. Nearly all of the components in the V/HTRs core are made of graphite material [4]. For example, the core of the pebble-bed reactor consists of a large number of graphite bricks with tenon holes, and the bricks are joined together by graphite tenons to form a complex structure. A large number of graphite balls and spherical fuel elements contained in the core are also wholly or partially made of graphite material. Hence, considering the extreme safety requirements of nuclear reactors, a safety evaluation of the reactor structures that considers the mechanical properties, failure modes and strength criterion for graphite material is crucial to the design and operation of V/HTRs [5,6]. Existing reports are mainly limited to the mechanical properties and failure modes of graphite material under simple stress conditions such as uniaxial tension or uniaxial compression [7–12]. Theories that have been applied to date include the maximum normal stress theory (the first strength theory) and maximum shear stress theory (the third strength theory), which only apply to simple stress states. However, due to the complex structures, the stress states of graphite material in a V/HTRs are extremely complex, such as the stress induced by the line contact between graphite tenon and graphite brick, and the stress induced by the point contact between graphite ball and graphite brick, or between graphite balls. In order to analyze the failure behaviors of graphite material under complex stress states, it would be very inappropriate to use the strength theories proposed for simple stress states. Therefore, it is necessary to study the strength criteria for graphite material under complex stress conditions, and the corresponding mechanical properties and failure modes. However, there is still a lack of literature on relevant studies.

It is well known that the mechanical properties, failure modes and strength criteria for materials under complex stress states are

* Corresponding author.
*E-mail address:* masp@bit.edu.cn (S. Ma).

https://doi.org/10.1016/j.net.2019.12.005
1738-5733/© 2019 Korean Nuclear Society, Published by Elsevier Korea LLC. This is an open access article under the CC BY-NC-ND license (http://creativecommons.org/licenses/by-nc-nd/4.0/).

quite different from those under simple stress state, especially for brittle materials. Taking rock-like brittle materials as an example, it has been found that their Young's moduli, peak strengths and some other rock material parameters increase with increasing confining pressure [13,14]. In addition, rock materials under uniaxial compression and low confining pressure exhibit a linear elastic stress-strain relationship and brittle failure characteristics. However, as the confining pressure increases, the failure modes gradually shift to compression-shear and plastic failure with significant volume expansion after the peak strength is reached [15,16]. Therefore, it can be inferred that the mechanical properties and failure modes of graphite material under confining pressure should also differ from those related to uniaxial loading. In order to predict the failure of rock materials, a wide variety of strength criteria were established by scholars based on different understandings of the strength characteristics of rock materials. Subsequently, in order to extend the practical applicability, the International Society of Rock Mechanics (ISRM) established a special research group, which proposed some famous strength criteria for rock materials and formulated the applicable conditions for each criterion to standardize its practical application [17]. These strength criteria include the Mohr-Coulomb criterion [18], the Hoek-Brown criterion [19], the 3D Hoek-Brown criterion [20], the Drucker-Prager criterion [21], the Lade and improved Lade criterion [22] and also failure criteria based on true triaxial experiments [23]. However, studies on the strength criteria for graphite material under different confining pressures are still scarce. With the rapid development of V/HTRs, there is an urgent need to find a suitable strength criterion for graphite material.

In consideration of the above-mentioned problems, a series of compressive failure tests were conducted by subjecting graphite material to different confining pressures in order to study the mechanical properties, failure modes and strength criteria for graphite material. In Section 2, the confining pressure tests are described in detail. In Section 3, the effects of confining pressure on the triaxial strength and Young's modulus of graphite material are discussed. The failure modes under different confining pressures were investigated by analyzing the fracture angles of the failed specimens, and further verified by evaluating the roughness of the fracture surfaces. In Section 4, different strength criteria are compared and a suitable one is identified for graphite material under different confining pressures. The concluding remarks are summarized in Section 5.

## 2. Experimental details

An isotropic graphite material, IG11, was selected as the experimental material in this study. IG11 is non-purified nuclear graphite IG110 and these two materials have quite similar mechanical properties. The specimens were 50 mm in diameter and 100 mm in height (Fig. 1). The confining pressures applied in this study were 0, 5, 10, 20, 30, and 40 MPa, with two specimens for each confining pressure. The confining pressures and detailed dimensions of all specimens are provided in Table 1.

**Table 1**
Confining pressures and specimen sizes.

| Specimen | Confining pressure (MPa) | Specimen size (mm) |
|---|---|---|
| #1 | 0 | $\phi$50.02 × 100.04 |
| #2 | | $\phi$50.04 × 100.00 |
| #3 | 5 | $\phi$50.00 × 100.00 |
| #4 | | $\phi$50.01 × 100.01 |
| #5 | 10 | $\phi$50.00 × 100.00 |
| #6 | | $\phi$50.02 × 100.01 |
| #7 | 20 | $\phi$50.01 × 100.02 |
| #8 | | $\phi$50.06 × 100.02 |
| #9 | 30 | $\phi$50.05 × 99.99 |
| #10 | | $\phi$50.01 × 100.00 |
| #11 | 40 | $\phi$50.06 × 100.00 |
| #12 | | $\phi$50.00 × 100.00 |

The tests were carried out by using a RLJW-2000 computer-controlled rock triaxial testing machine. The radial loading on the specimens was stress controlled, and the axial loading was displacement controlled. The radial and axial displacements were recorded by using a deformation sensor matching with the testing machine (Fig. 2). The deformation sensor is composed of eight cantilever beam extensometers, four long ones for axial displacement measurement and four short ones for radial displacement measurement. The upper ladder head of the deformation sensor is fixed to the upper indenter of the testing machine by bolts and the lower base is fixed to the lower indenter. The upper indenter always contacts with the top surface of the specimen. During the loading process, the upper indenter keeps fixed and the lower indenter moves upward. This will cause the long cantilever beams to deflect along the upper ladder head and the deflections can be obtained by the strain gauges located near to the roots of the cantilever beams. After averaging the four deflection values, the axial displacement of the specimen can be calculated according to the relationship between the deflection of the cantilever beam and the axial displacement of the specimen. Similarly for the radial displacement measurement, the bolts on the radial deformation extensometers are in close contact with the specimen. When the specimen deforms in radial direction, the bolts will move outward and cause the cantilever beams to deflect. Based on the strains measured by the strain gauges, the deflections of the cantilever beams and then the radial displacement of the specimen can be obtained.

Before the experiments, the surfaces of each specimen were cleaned by alcohol and then air-dried. The testing procedure includes four steps (Fig. 3). Firstly, the top and bottom surfaces of the specimen were connected to the upper and lower indenters,

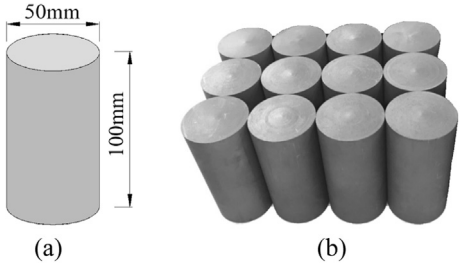


**Fig. 1.** Graphite specimens: (a) Specimen geometry, (b) Picture of specimens.

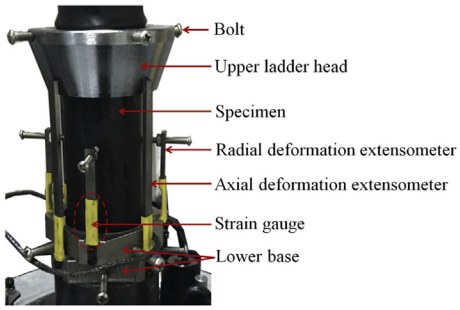


**Fig. 2.** Deformation sensor for axial and radial displacement measurements.

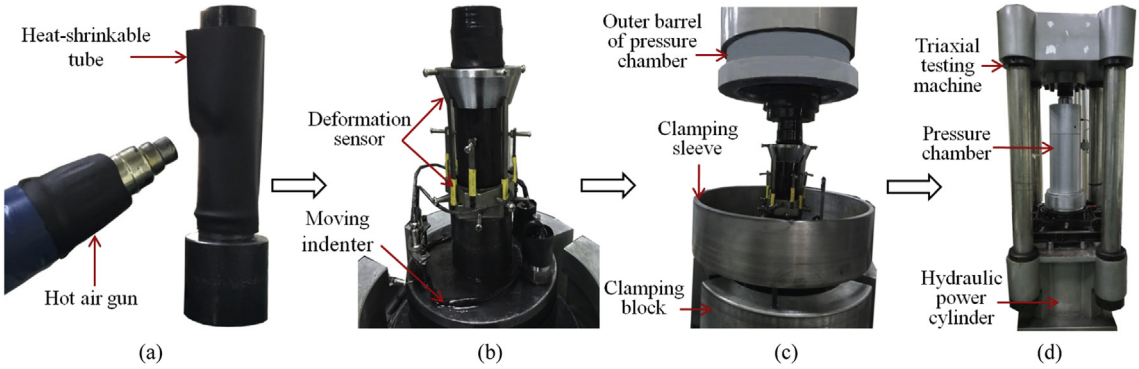


**Fig. 3.** Experimental procedure: (a) Cover heat-shrinkable tubes, (b) Install and adjust deformation sensors, (c) Place the specimen on the testing machine, and (d) Start the test.

respectively. Two layers of heat-shrinkable tubes were baked onto the specimen by a hot air gun (Fig. 3 (a)) and the purpose of putting the second layer is to prevent the specimen from being immersed in the hydraulic oil in case the first layer was damaged by the failed specimen. Secondly, the deformation sensor was installed on the specimen (Fig. 3 (b)). Thirdly, the assembled components including the specimen, the heat-shrinkable tubes, the deformation sensor and the indenters were properly placed on the triaxial testing machine (Fig. 3 (c)). Finally, a closed pressure chamber was installed (Fig. 3 (d)). The confining pressure and the axial pressure were synchronously increased to the desired pressure at a loading rate of 0.05 MPa/s to make the specimen in a hydrostatic pressure state. In other words, the hydrostatic pressure is preloaded to the specimen. After the confining pressure was stabilized, the axial loading was increased at a loading rate of 0.1 mm/min until the specimen failed. During the experiment, the amount of oil in the pressure chamber was slightly adjusted to keep the confining pressure constant.

## 3. Results and analysis

### 3.1. Mechanical properties

The experimental results for graphite material are outlined in Table 2 for various confining pressures. $\sigma_3$ is the confining pressure, namely, the second and third principal stresses; $\sigma_1^c$ is the triaxial compressive strength; $\overline{\sigma_1^c}$ is the average triaxial compressive strength; $\overline{\sigma_1^c - \sigma_3}$ is the average critical deviatoric stress; $\varepsilon_1^c$ is the axial failure strain, which does not include the axial strain generated by the hydraulic pressure; $\overline{\varepsilon_1^c}$ is the average axial failure strain; $\varepsilon_3^c$ is the radial failure strain, which does not include the radial strain generated by the hydraulic pressure; $\overline{\varepsilon_3^c}$ is the average radial failure strain. It can be seen from Table 2 that increasing the confining pressure from 0 to 40 MPa resulted in increases of the average triaxial compressive strength from 67.0 to 128.0 MPa (1.9 times), the average axial failure strain from 0.024 to 0.097 (4.0 times) and the absolute average of radial failure strain from 0.006 to 0.019 (3.2 times). This means that the triaxial compressive strength and failure strain of graphite material were remarkably enhanced by increasing the confining pressure.

The deviatoric stress-strain curves are shown in Fig. 4 for all graphite specimens. It can be seen that, when the axial strain and radial strain were small, the deviatoric stress-strain curves were nearly linear. With the increase of the axial or radial strain, the curves deviated from linearity. The specimens failed suddenly and the stresses dropped abruptly after the peak strengths were reached. For cases with the confining pressure in the range of 5–40 MPa, the graphite specimens did not exhibit any obvious ductile flow characteristics. This phenomenon is different from those of rocks [24,25]. With the increase of confining pressure, rock specimens do not show obvious failure precursors, and present obvious ductile flow characteristics. Rock materials usually show softening after the peak strengths in their deviatoric stress-strain curves, and the larger the confining pressure, the smaller the absolute value of the softening slope. When the confining pressure is high enough, the softening curve may even flatten. Further study on the relationship between the triaxial compressive strength and confining pressure of the graphite material (Fig. 5) showed that the triaxial compressive strength gradually increased as the confining pressure was increased.

**Table 2**
Failure strength and strain values for graphite specimens under different confining pressures.

| Specimen | $\sigma_3$ (MPa) | $\sigma_1^c$ (MPa) | $\overline{\sigma_1^c}$ (MPa) | $\overline{\sigma_1^c - \sigma_3}$ (MPa) | $\varepsilon_1^c$ | $\overline{\varepsilon_1^c}$ | $\varepsilon_3^c$ | $\overline{\varepsilon_3^c}$ |
|---|---|---|---|---|---|---|---|---|
| #1 | 0 | 65.5 | 67.0 | 67.0 | 0.022 | 0.024 | −0.005 | −0.006 |
| #2 | | 68.4 | | | 0.026 | | −0.006 | |
| #3 | 5 | 79.9 | 80.1 | 75.1 | 0.033 | 0.034 | −0.007 | −0.008 |
| #4 | | 80.3 | | | 0.035 | | −0.008 | |
| #5 | 10 | 88.0 | 87.6 | 77.6 | 0.043 | 0.042 | −0.009 | −0.009 |
| #6 | | 87.1 | | | 0.041 | | −0.009 | |
| #7 | 20 | 103.6 | 104.1 | 84.1 | 0.067 | 0.067 | −0.013 | −0.014 |
| #8 | | 104.6 | | | 0.066 | | −0.015 | |
| #9 | 30 | 112.8 | 113.4 | 83.4 | 0.071 | 0.077 | −0.014 | −0.016 |
| #10 | | 114.0 | | | 0.083 | | −0.018 | |
| #11 | 40 | 127.9 | 128.0 | 88.0 | 0.097 | 0.097 | −0.019 | −0.019 |
| #12 | | 128.1 | | | 0.096 | | −0.018 | |

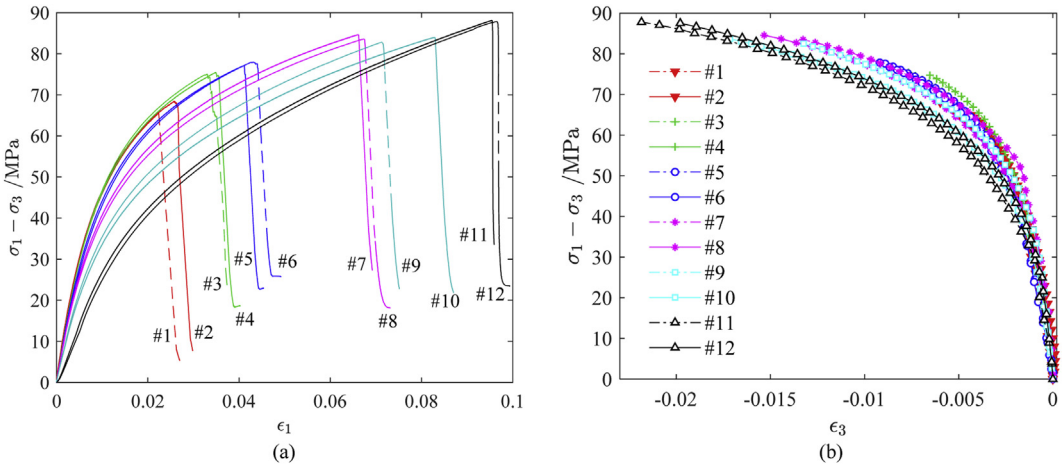


**Fig. 4.** The deviatoric stress-strain curves: (a) Deviatoric stress versus axial strain, (b) Deviatoric stress versus radial strain.

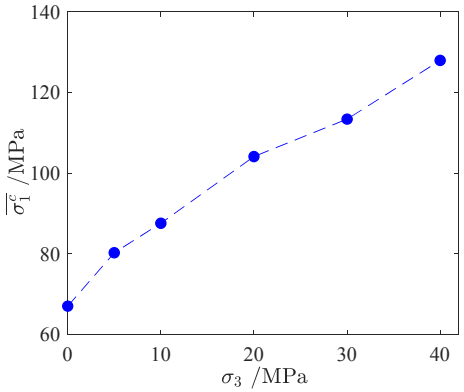


**Fig. 5.** Triaxial compressive strength versus confining pressure.

In this study, the Young's modulus $E^*$ of the graphite material under confining pressure was specifically defined as the ratio of the deviatoric stress to the axial strain as follows:

$$E^* = \overline{\sigma_1 - \sigma_3} / \varepsilon_1 \quad (1)$$

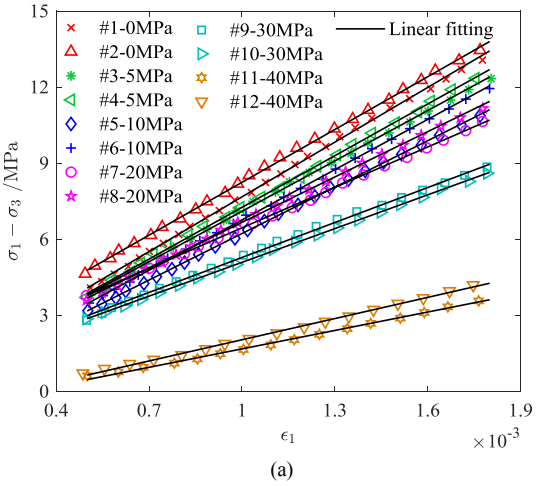


**Fig. 6.** The Young's modulus fitting results for graphite material subjected to different confining pressures.

This modulus can be considered as a mechanical property of the graphite material under a specific confining pressure. In this study, the data for the deviatoric stress-strain curves in the early loading stage (i.e., axial strain range of 0.0005–0.0018) were selected for linear curve fitting (Fig. 6). The fitted results are shown in Table 3, in which $\overline{E^*}$ is the average Young's modulus for the two specimens under the same confining pressure. It can be seen from the Young's modulus-confining pressure curves in Fig. 7 that the Young's modulus of the graphite material gradually decreased with the increase of the confining pressure. This experimental result is contrary to those of rocks, whose Young's modulus increased with the increase of the confining pressure [25–27]. The exact reason for this contradiction needs to be elucidated by a future research work.

### 3.2. Failure modes

The failed graphite specimens under different confining pressures are shown in Fig. 8. Each failure diagram shows the front and back of a specimen with the main cracks parallel to the out-of-plane direction. The failure diagrams were processed to highlight the characteristics of the fracture planes. It can be seen that the failure modes of the graphite specimens under confining pressure significantly differ from that of the specimen under uniaxial compression (Fig. 8 (a)). Without confining pressure, the graphite specimens were failed by severe fragmentation and multiple cracks. Since the main cracks are nearly parallel to the loading direction, the failure mode is considered to be tension dominated. When the confining

**Table 3**
Young's modulus for different confining pressures.

| Specimen | $\sigma_3$ (MPa) | $E^*$ (GPa) | $\overline{E^*}$ (GPa) |
|---|---|---|---|
| #1 | 0 | 7.19 | 7.1 |
| #2 | | 6.94 | |
| #3 | 5 | 6.62 | 6.7 |
| #4 | | 6.79 | |
| #5 | 10 | 6.10 | 6.4 |
| #6 | | 6.61 | |
| #7 | 20 | 5.32 | 5.6 |
| #8 | | 5.96 | |
| #9 | 30 | 4.60 | 4.5 |
| #10 | | 4.44 | |
| #11 | 40 | 2.42 | 2.6 |
| #12 | | 2.79 | |

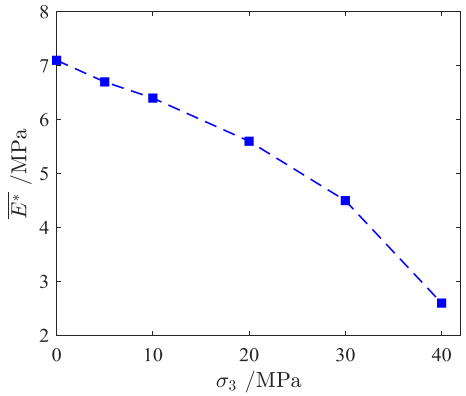


**Fig. 7.** Young's modulus versus confining pressure.

pressure was increased to 5 MPa, the number of cracks and the degree of fragmentation of the graphite specimens significantly decreased, and a cone was formed by the main cracks (Fig. 8 (b)). Basically, the specimens exhibited a shear-tension failure mode with tension failure as the main factor and shear failure as the auxiliary one. As the confining pressure continued to increase, the number of cracks decreased until there is only a single and neat fracture plane (Fig. 8 (c–f)). When the confining pressure was 10 or 20 MPa, the main crack passed through the upper and lower surfaces of the specimens, which implies a tension-shear failure mode that is dominated by shear failure and supplemented by tension failure (Fig. 8 (c) and (d)). When the confining pressure was 30 or 40 MPa, the crack propagated from one end to the side of the specimens, and the specimens failed by a shear failure mode (Fig. 8 (e) and (f)). The fracture angle ($\theta$), which is defined as the angle between the fracture and horizontal planes, was also calculated for each specimen. It can be seen from Table 4 that the average fracture angle ($\overline{\theta}$) decreased from 86.1° to 59.4° as the confining pressure was increased and there was a linear relationship between the fracture angle and the confining pressures within the range of 5–40 MPa (Fig. 9).

The change of failure modes of graphite specimens with increasing confining pressures can be verified by the roughness of the fracture surfaces. In this study, a micron-scale laser measuring system was used to evaluate the fracture surface morphology (Fig. 10 (a)). For each specimen, a proper scanning area (10 mm × 10 mm) in the middle of the fracture surface was scanned (Fig. 10 (b)). The sampling was performed along x direction (slip direction) on the fracture surface at a speed of 0.2 mm/s and sampling frequency of 784 Hz. The scanning step size in y direction (perpendicular to the slip direction) was 0.2 mm and there were totally 51 samples for each specimen (Fig. 11 (a)). Four steps were used to process the data for each sample and calculate the roughness of the fracture surface. Firstly, each sample (Fig. 11 (b)) was divided into multiple subsamples (Fig. 11 (c)). To capture the tiny peaks and valleys on the specimen surface, the size of the subsamples should be small enough and was chosen as 0.4 mm in this study. Secondly, the middle line of the contour of each subsample was determined by using the least square method (Fig. 11 (c)), and the perpendicular distance of each point in the subsample to the middle line was calculated. Thirdly, the arithmetic mean of the perpendicular distances of all points in the subsample was calculated by Eq. (2) and taken as the roughness parameter of the subsample:

$$R_a^{'} = \frac{1}{n}\sum_{i=1}^{n}|z(x_i)| \tag{2}$$

where $n$ is the number of points in the subsample, and $z(x_i)$ is the perpendicular distance of each point to the middle line of the subsample contour. Finally, the roughness parameters $R_a^{'}$ of all subsamples in the scanning area were averaged to obtain the roughness $R_a$ of the fracture surface.

The roughness $R_a$ and standard deviations $S_a$ of failed specimens under different confining pressures are shown in Table 5. Fig. 12 shows the roughness as a function of the confining pressure. The high roughness at low confining pressure indicates that the failure was tension dominated, and the low roughness at high confining pressure indicates that the failure was shear dominated because a frictional slip resulted in relatively smooth fracture surfaces. In summary, with the increase of confining pressure, the failure modes of graphite specimens changed from tension-dominated failure to shear-dominated failure.

## 4. Strength criterion

In this paper, the suitable strength criterion for graphite IG11 was studied by referring to the most famous strength criteria for

**Table 4**
Fracture angles for different confining pressures.

| Specimen | $\sigma_3$ (MPa) | $\theta$ (°) | $\overline{\theta}$ (°) |
|---|---|---|---|
| #1 | 0 | 87.1 | 86.1 |
| #2 | | 85.0 | |
| #3 | 5 | 68.7 | 67.7 |
| #4 | | 66.7 | |
| #5 | 10 | 67.2 | 67.0 |
| #6 | | 66.7 | |
| #7 | 20 | 63.4 | 63.5 |
| #8 | | 63.5 | |
| #9 | 30 | 61.5 | 62.0 |
| #10 | | 62.5 | |
| #11 | 40 | 59.5 | 59.4 |
| #12 | | 59.2 | |

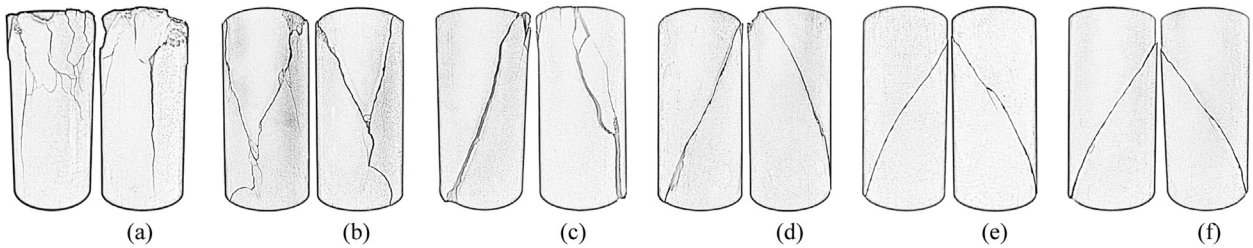


**Fig. 8.** Failure diagrams showing the front and back sides of the specimens with the main cracks parallel to the out-of-plane direction: (a) 0 MPa, (b) 5 MPa, (c) 10 MPa, (d) 20 MPa, (e) 30 MPa, and (f) 40 MPa.

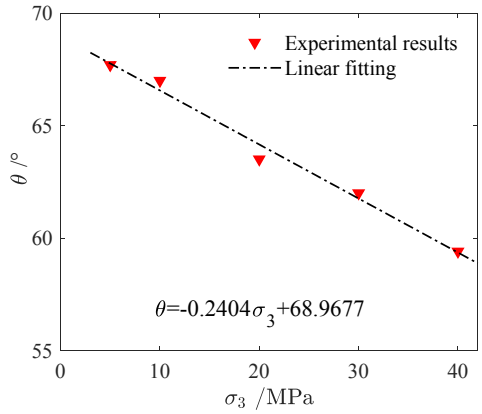


**Fig. 9.** Fracture angle versus confining pressure.

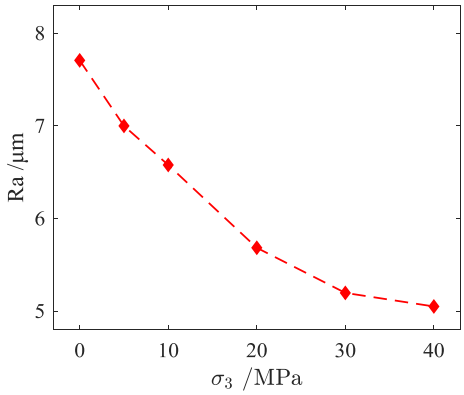


**Fig. 12.** Fracture surface roughness versus confining pressure.

rock materials proposed by the International Society of Rock Mechanics (ISRM) [17]. These strength criteria include the Mohr-Coulomb criterion [18], the Hoek-Brown criterion [19], the 3D Hoek-Brown criterion [20] and the Drucker-Prager criterion [21]. The equations of these strength criteria are shown in Table 6. The parameters in these equations can be determined experimentally or empirically for the graphite material. According to the Mohr-Coulomb criterion (Eq. (3)), the internal friction angle ($\varphi$) and cohesive force ($c$) of the graphite material can be calculated by using the experimental results given in Table 2, and they are $\varphi = 10.64°$ and $c = 29.58$ MPa. The uniaxial compressive strength is $\sigma_c = 67.0$ MPa based on the uniaxial compression test (Table 2). The

**Table 5**
Roughness of fracture surfaces of specimens for different confining pressures.

| $\sigma_3$ (MPa) | $R_a$ (μm) | $S_a$ (μm) |
|---|---|---|
| 0 | 7.71 | 6.90 |
| 5 | 7.00 | 7.06 |
| 10 | 6.58 | 6.30 |
| 20 | 5.68 | 5.71 |
| 30 | 5.20 | 5.21 |
| 40 | 5.05 | 5.51 |

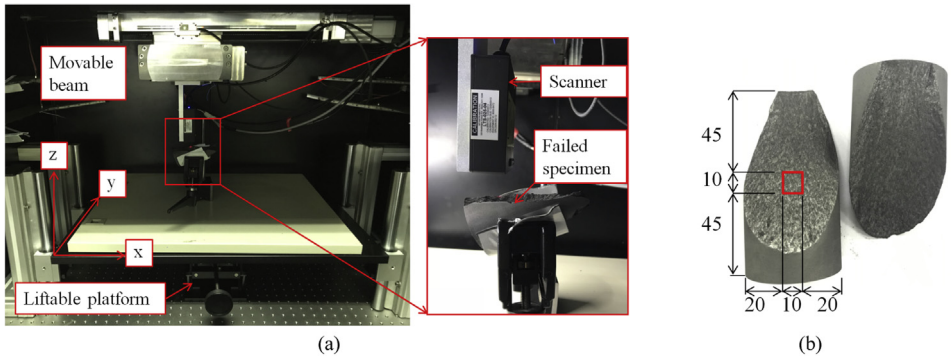


**Fig. 10.** Fracture surface roughness measurement: (a) Experimental setup, and (b) Scanning area (Unit: mm).

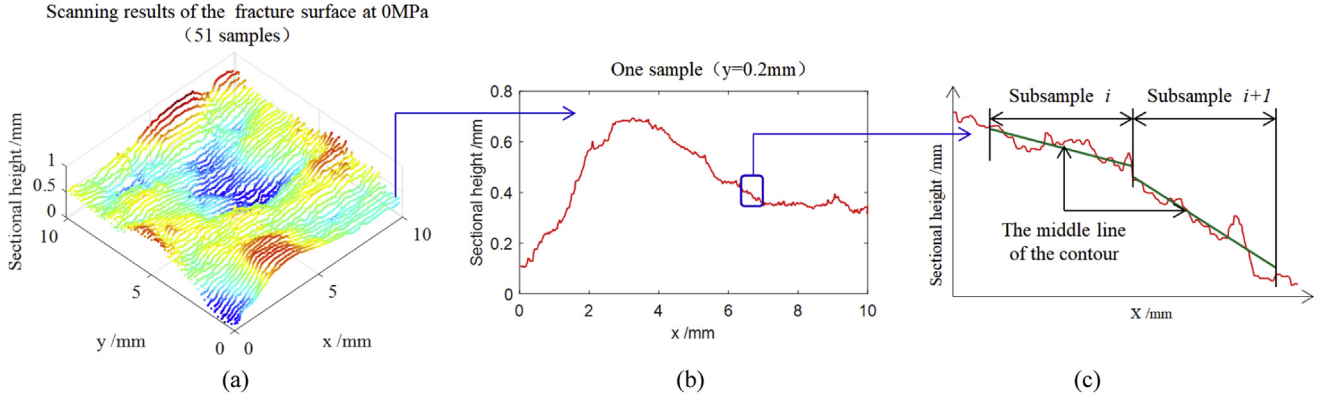


**Fig. 11.** Scanned area sample and subsample results.

**Table 6**
Equations of strength criteria for rock materials.

| Criterion | Equation | Number |
|---|---|---|
| Mohr-Coulomb criterion | $\sigma_1 = \xi\sigma_3 + \sigma_c$<br>Where $\xi = \frac{1+\sin\varphi}{1-\sin\varphi}$, and $\sigma_c = \frac{2c\cdot\cos\varphi}{1-\sin\varphi}$. | Eq. (3) |
| Hoek-Brown criterion | $\sigma_1 = \sigma_3 + \sigma_c\left(m_b\frac{\sigma_3}{\sigma_c} + s\right)^a$<br>where $a = \frac{1}{2} + \frac{1}{6}\left(\exp\left(\frac{-GSI}{15}\right) + \exp\left(\frac{-20}{3}\right)\right)$, $m_b = m_i\exp\left(\frac{GSI-100}{28-14D}\right)$ and $s = \exp\left(\frac{GSI-100}{9-3D}\right)$. | Eq. (4) |
| 3D Hoek-Brown criterion | $s\sigma_c = \sigma_c^{\left(1-\frac{1}{a}\right)}\left(\frac{3\tau_{oct}}{\sqrt{2}}\right)^{\frac{1}{a}} + \frac{3m_b\tau_{oct}}{2\sqrt{2}} - \frac{m_b(I_1-\sigma_2)}{2}$<br>Where $a$, $m_b$ and $s$ are the same as Eq. (4), $\tau_{oct} = \frac{1}{3}\sqrt{(\sigma_1-\sigma_2)^2+(\sigma_2-\sigma_3)^2+(\sigma_3-\sigma_1)^2}$, $I_1 = \sigma_1+\sigma_2+\sigma_3$. | Eq. (5) |
| Drucker-Prager criterion | $\sqrt{J_2} = \alpha I_1 + k$<br>where $J_2 = \frac{1}{6}[(\sigma_1-\sigma_2)^2+(\sigma_2-\sigma_3)^2+(\sigma_3-\sigma_1)^2]$, $\alpha = \frac{2\sin\varphi}{\sqrt{3}(3-\sin\varphi)}$ and $k = \frac{6c\cdot\cos\varphi}{\sqrt{3}(3-\sin\varphi)}$. | Eq. (6) |

geological strength index ($GSI$) is a system of rock-mass characterization that has been developed in engineering rock mechanics, and the value of $GSI = 100$ was used in this work based on the surface conditions of the graphite specimens [28]. Factor $D$ depends on the degree of disturbance due to blast damage and stress relaxation, and the value of $D = 0$ was used in this work because the graphite material is undisturbed [29]. Factor $m_i$ is a material constant which depends upon the rock type (texture and mineralogy) [30–32], and the value of $m_i = 1.5$ was used for the graphite material after a parametric analysis to make the prediction close to the experimental results.

Fig. 13 shows the curves of the four strength criteria in Table 6 for the graphite material. It can be seen that the prediction by the Drucker-Prager criterion deviated significantly from the experimental results. Comparatively, the predictions by the Hoek-Brown criterion, the 3D Hoek-Brown criterion and the Mohr-Coulomb criterion were in good agreement with the experimental results. However, the equations of the Hoek-Brown criterion and the 3D Hoek-Brown criterion contain some unknown parameters which are difficult to be determined. Therefore, these two criteria are not recommended and the Mohr-Coulomb criterion is preferred in strength evaluation for the graphite material.

The Mohr circles for graphite IG11 at failure under different confining pressures were drawn in Fig. 14. When considering the tensile strength (27.6 MPa) of graphite IG11 measured from a ring compression test [12], i.e., the Mohr circle for negative $\sigma$ in Fig. 14, the linear Mohr-Coulomb criterion may not be adequate for strength prediction of graphite IG11 and it is necessary to consider the non-linear form [33]. According to the experimental results given in Table 2 and the tensile strength, the parabolic Mohr-Coulomb criterion can be fitted as follows:

$$\sigma = 0.05\tau^2 - 27.60 \tag{7}$$

In the $\sigma$-$\tau$ coordinate system, the Mohr-Coulomb criterion (Eq. (3)) can be expressed by the internal friction angle and cohesion as follows:

$$\tau = \sigma tan10.64^\circ + 29.58 \tag{8}$$

From the Mohr circles, the Mohr strength envelope was obtained (the red dash line I in Fig. 14). The curves for the Mohr-Coulomb criterion (Eq. (8)) and parabolic Mohr-Coulomb criterion (Eq. (7)) were also drawn by blue dash dot line II and green solid line III, respectively. It can be easily seen that the Mohr-Coulomb criterion significantly deviated from the Mohr strength envelope, and the parabolic Mohr-Coulomb strength criterion was more consistent with the Mohr strength envelope.

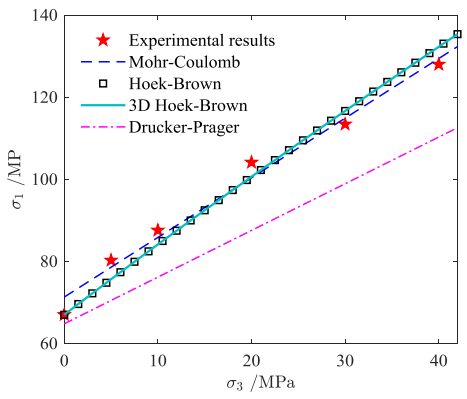


**Fig. 13.** Results of the four strength criteria.

## 5. Conclusion

To better understand the mechanical behavior of graphite material, the effects of confining pressure on its mechanical properties, failure modes, and strength criteria were investigated. The mechanical behavior under confining pressure was found to be very different from that under uniaxial compression. The following conclusions can be made from the test results:

(1) By increasing the confining pressure, the triaxial compressive strength and failure strain of the graphite material significantly increased. Moreover, higher confining pressure corresponded to more serious damage within the nuclear graphite and a smaller Young's modulus, which is contrary to the phenomenon observed for rock materials.
(2) By increasing the confining pressure, the graphite material exhibited four types of failure modes in order: tension failure, shear-tension failure, tension-shear failure and shear failure, and meanwhile the fracture surface roughness gradually decreased.
(3) Different strength criteria were compared and the Mohr-Coulomb strength criterion was found to be more suitable for the graphite material. Based on the Mohr circles of the graphite material, the parabolic Mohr-Coulomb criterion is more consistent with the Mohr strength envelope than the

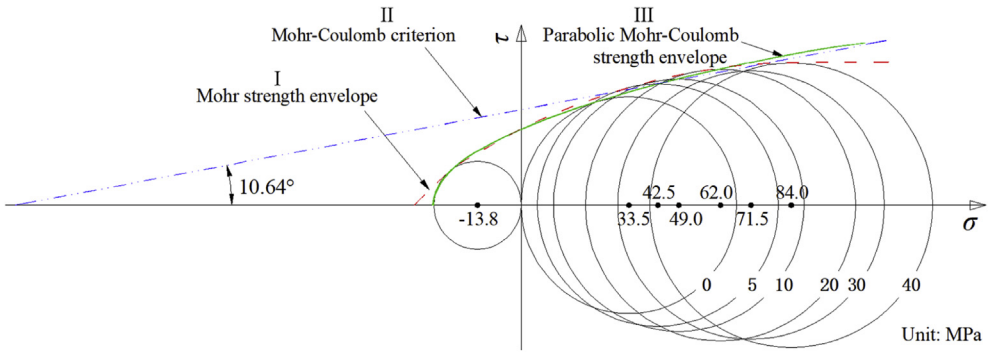


**Fig. 14.** Strength envelope and criteria for graphite IG11.

linear Mohr-Coulomb criterion and should be used for graphite strength predictions.

## Declaration of competing interest

The authors declare that they have no known competing financial interests or personal relationships that could have appeared to influence the work reported in this paper.

## Acknowledgements

This study was supported by the National Natural Science Foundation of China (Grant Nos. 11872115, U1837602, 11727801, 11772053 and 11602022), the National S&T Major Project (Grant Nos. ZX06901 and ZX06907), and the opening projects from the State Key Laboratory of Earthquake Dynamics (Grant No. LED2016B02). The authors would also like to thank Dr. Yanchun Yin and Mr. Bin Huang for their help with the experiments.

## Appendix A. Supplementary data

Supplementary data to this article can be found online at https://doi.org/10.1016/j.net.2019.12.005.

## References

[1] S.P. Jing, C. Zhang, J. Pu, H.Y. Jiang, H.H. Xia, F. Wang, X. Wang, 3D microstructures of nuclear graphite: IG-110, NBG-18 and NG-CT-10, Nucl. Sci. Tech. 27 (2016) 1–8.
[2] G. Singh, A. Fok, S. Mantell, Failure predictions for graphite reflector bricks in the very high temperature reactor with the prismatic core design, Nucl. Eng. Des. 317 (2017) 190–198.
[3] X.W. Zhou, Y.P. Tang, Z.M. Lu, J. Zhang, B. Liu, Nuclear graphite for high temperature gas-cooled reactors, N. Carbon Mater. 32 (2017) 193–204.
[4] Z.X. Wu, D.C. Lin, D.X. Zhong, The design features of the HTR-10, Nucl. Eng. Des. 218 (2002) 25–32.
[5] Z.X. Wu, The module HTGR development in China, Eng. Sci. 4 (2007) 59–67.
[6] X.W. Zhou, Y. Yang, J. Song, Z.M. Lu, J. Zhang, B. Liu, Y.P. Tang, Carbon materials in a high temperature gas-cooled reactor pebble-bed module, N. Carbon Mater. 33 (2018) 97–108.
[7] A. Cosculluela, J. Farre, Uniaxial compressive behaviour of an isotropic graphite, J. Phys. IV 7 (1997) 471–476.
[8] R. Taylor, R.G. Brown, K. Gilchrist, E. Hall, A.T. Hodds, B.T. Kelly, F. Morris, The mechanical properties of reactor graphite, Carbon 5 (1967) 519–531.
[9] M.P. Hindley, M.N. Mitchell, D.C. Blaine, A.A. Groenwold, Observations in the statistical analysis of NBG-18 nuclear graphite strength tests, J. Nucl. Mater. 420 (2012) 110–115.
[10] A.R. Shahani, M.M. Nejadi, Investigation on the mechanical properties and fracture toughness of graphite, FFEMS 38 (2015) 1209–1218.
[11] A.P.G. Rose, M.O. Tucker, A fracture criterion for nuclear graphite, J. Nucl. Mater. 110 (1982) 186–195.
[12] X.J. Zhang, Y.N. Yi, H.B. Zhu, G.Y. Liu, L.B. Sun, L. Shi, H. Jiang, S.P. Ma, Measurement of tensile strength of nuclear graphite based on ring compression test, J. Nucl. Mater. 511 (2018) 134–140.
[13] J. Arzua, L.R. Alejano, G. Walton, Dilation in granite during servo-controlled triaxial strength tests, Int. J. Rock Mech. Min. 61 (2013) 43–56.
[14] S.Q. Yang, Y.Z. Jiang, W.Y. Xu, X.Q. Chen, Experimental investigation on strength and failure behavior of pre-cracked marble under conventional triaxial compression, Int. J. Solids Struct. 45 (2008) 4796–4819.
[15] M.Q. You, Mechanical characteristics of the exponential strength criterion under conventional triaxial stresses, Int. J. Rock Mech. Min. 47 (2010) 195–204.
[16] B. Tarasov, Y. Potvin, Universal criteria for rock brittleness estimation under triaxial compression, Int. J. Rock Mech. Min. 59 (2013) 57–69.
[17] B. Haimson, A. Bobet, Introduction to suggested methods for failure criteria, Rock Mech. Rock Eng. 45 (2012) 973–974.
[18] J.F. Labuz, A. Zang, Mohr-Coulomb failure criterion, Rock Mech. Rock Eng. 45 (2012) 975–979.
[19] E. Eberhardt, The Hoek–Brown failure criterion, Rock Mech. Rock Eng. 45 (2012) 981–988.
[20] S. Priest, Three-dimensional failure criteria based on the Hoek–Brown criterion, Rock Mech. Rock Eng. 45 (2012) 989–993.
[21] L.R. Alejano, Drucker-Prager criterion, Rock Mech. Rock Eng. 45 (2012) 995–999.
[22] S.A.B. Da Fontoura, Lade and modified Lade 3D rock strength criterion, Rock Mech. Rock Eng. 45 (2012) 1001–1006.
[23] C.D. Chang, B. Haimson, A failure criterion for rocks based on true triaxial testing, Rock Mech. Rock Eng. 45 (2012) 1007–1010.
[24] S.Q. Yang, Y.Z. Jiang, W.Y. Xu, X.Q. Chen, Experimental investigation on strength and failure behavior of pre-cracked marble under conventional triaxial compression, Int. J. Solids Struct. 45 (2008) 4796–4819.
[25] L. Yong, Effect analysis of confining pressure on Young's modulus, J. Chongqing Jianzhu Univ. 28 (2009) 246–249. In Chinese.
[26] W.R. Wawersik, W.F. Brace, Post failure behavior of a granite and a diabase, Rock Mech. 3 (1971) 61–85.
[27] M.Q. You, Effect of confining pressure on the Young's modulus of rock specimen, Chin. J. Rock Mech. Eng. 22 (2003) 53–60. In Chinese.
[28] V. Marinos, P. Marinos, E. Hoek, The geological strength index: applications and limitations, Bull. Eng. Geol. Environ. 64 (2005) 55–65.
[29] L. Zhang, A generalized three-dimensional Hoek-Brown, Rock Mech. Rock Eng. 41 (2008) 893–915.
[30] Q. Zhang, H. Zhu, L. Zhang, Modification of a generalized three-dimensional Hoek-Brown strength criterion, Int. J. Rock Mech. Min. 59 (2013) 80–96.
[31] E. Hoek, E.T. Brown, Practical estimates of rock mass strength, Int. J. Rock Mech. Min. 34 (1997) 1165–1186.
[32] P. Marinos, E. Hoek, Estimating the geotechnical properties of heterogeneous rock masses such as flysch, Bull. Eng. Geol. Environ. 60 (2001) 85–92.
[33] C.G. Li, X.R. Ge, H. Zheng, S.L. Wang, Two-parameter parabolic Mohr strength criterion and its damage regularity, Key Eng. Mater. 306 (2006) 327–332.